Available online at www.sciencedirect.com
SCIENCE DIRECT®
Comput. Methods Appl. Mech. Engrg. 194 (2005) 3291–3314
Computer methods in applied mechanics and engineering
www.elsevier.com/locate/cma

Eulerian shape design sensitivity analysis and optimization with a fixed grid

Nam H. Kim *, Youngmin Chang

Department of Mechanical and Aerospace Engineering, University of Florida, P.O. Box 116250, Gainesville, FL 32611-6250, USA

Received 20 January 2004; received in revised form 8 June 2004; accepted 6 December 2004

Abstract

Conventional shape optimization based on the finite element method uses Lagrangian representation in which the finite element mesh moves according to shape change, while modern topology optimization uses Eulerian representation. In this paper, an approach to shape optimization using Eulerian representation such that the mesh distortion problem in the conventional approach can be resolved is proposed. A continuum geometric model is defined on the fixed grid of finite elements. An active set of finite elements that defines the discrete domain is determined using a procedure similar to topology optimization, in which each element has a unique shape density. The shape design parameter that is defined on the geometric model is transformed into the corresponding shape density variation of the boundary elements. Using this transformation, it has been shown that the shape design problem can be treated as a parameter design problem, which is a much easier method than the former. A detailed derivation of how the shape design velocity field can be converted into the shape density variation is presented along with sensitivity calculation. Very efficient sensitivity coefficients are calculated by integrating only those elements that belong to the structural boundary. The accuracy of the sensitivity information is compared with that derived by the finite difference method with excellent agreement. Two design optimization problems are presented to show the feasibility of the proposed design approach.

Keywords: Shape optimization; Topology optimization; Boundary homogenization; Design sensitivity analysis; Fixed grid

1. Introduction

For three decades, remarkable progress has been achieved in geometry-based structural shape optimization [1]. Shape optimization techniques have been successfully integrated with CAD tools, so that design

* Corresponding author. Tel.: +1 352 846 0665; fax: +1 352 392 7303.
E-mail address: nkim@ufl.edu (N.H. Kim).

0045-7825/$ - see front matter
doi:10.1016/j.cma.2004.12.019

variables are chosen from CAD parameters, providing consistency between the design and CAD models [2,3]. A major problem of geometry-based shape optimization is the mesh distortion problem during structural analysis [4]. The regularly distributed mesh at the initial design is often distorted during shape optimization, and as a result, solution accuracy of finite element analysis deteriorates after the initial design. Although many adaptive mesh-regeneration methods have been studied in order to maintain a certain level of solution accuracy, they produce discontinuities in the objective and/or constraints, thus possibly making gradient based optimization complicate [4]. In this paper, conventional shape optimization is referred to as the Lagrangian method since both the geometry and finite element mesh move together during the shape optimization process.

In contrast to the Lagrangian method, a topology optimization method has been developed in order to determine the optimum structural shape without causing any mesh distortion problems [5,6]. The initial geometry of the finite element mesh is maintained throughout the design process, and the material property (shape density) of each element changes as a design variable changes. However, an excessive number of design variables make it difficult to find the optimum design, and results in too many local optimum solutions. In addition, the practicality of the optimum design often raises questions as to the feasibility of manufacturing a structure based on the optimum design. It is non-trivial to determine the structural boundary shape from topology optimization results. In contrast to the shape design, this approach is referred to as the Eulerian method since the shape of the finite element mesh is fixed during the design process.

In this paper, a shape optimization method within the fixed grid framework that uses the efficiency of the adjoint method in the shape sensitivity analysis problem and the advantageous aspects of both conventional shape and topology optimization methods is proposed. The Lagrangian method has the advantage of accurately representing the geometric model, while the Eulerian method relieves mesh distortion problems. During structural analysis, the geometric model is placed over regularly meshed finite elements. The finite elements are fixed during the design process, while the geometric model changes according to the shape design. Finite elements that belong inside the geometric model have a full magnitude of shape density, while those outside the model have a zero magnitude of shape density (a void). Finite elements on the geometric edge have a shape density that is proportional to the area fraction between the material and void. Thus, finite elements on the edge have a shape density between full material and a void. This method is similar to the homogenization method in topology optimization. Thus, in this paper it is referred to as boundary homogenization.

A similar methodology has appeared in the literature. García and Steven [7] applied fixed grid finite element analysis to elasticity problems. Even if the displacement and stress at the boundary oscillate due to the element location to the boundary curve, García and Steven showed that the error reduces as the size of the finite element decreases. They also used the least square method to approximate the stress on the boundary. Using the fixed grid analysis capability, García and Steven also developed design optimization using a fast re-analysis method, which is similar to the discrete semi-analytical method in sensitivity analysis [8,9]. Recently, Woon et al. [10] applied the fixed grid approach to shape optimization using the genetic algorithm, and Kim et al. [11] applied the fixed grid approach to the evolutionary structural optimization (ESO) problem. The ESO process is started by generating a stiffness matrix of the given initial design. Once the matrix is defined, it is solved for displacement and the stress values of each element. ESO then physically removes a small percentage of elements that have low stress values. This completes one cycle of the ESO process. Repeating this process leads to the optimum design. However, the disadvantages of ESO are the expensive solution cost due to the iterative and slow nature of the ESO process. Implementing the fixed grid methodology not only simplifies the mesh generation process, but also allows a very significant reduction of the arithmetic calculations necessary to update the stiffness matrix for the modified topology, instead of a full regeneration of the matrix.

In shape optimization, a shape change in the geometric model produces a shape density change in the finite elements on the edge. As the structural shape changes, a new shape density is calculated for the ele-

ments on the edge. In addition, some elements leave the structural domain, while others enter it. Thus, accurate record keeping of each stage is an important part of the proposed approach. First, the finite elements that belong to the boundary curve are identified by an incremental searching of the boundary curve. After identifying these elements, an area fraction of each boundary element is calculated using Green's theorem. Finite elements within the structural domain can easily be identified by counting the number of boundary elements in each row or column of the grid. As opposed to Lagrangian shape representation, this approach does not require a mesh updating process.

In the Lagrangian shape design, the design variable derives the boundary shape design velocity field, which represents the motion of the boundary curve according to the design variable. However, one mathematical difficulty with the proposed method is to find a way to represent the effect of shape change as shape density changes. Since shape design variables are chosen from geometric parameters, the explicit contribution of the boundary curve shape to the shape density of the boundary element is calculated based on geometric relations. Accordingly, boundary shape design velocity is related to the shape density of the boundary elements, which is used in design sensitivity calculation. Thus, the complicated shape design sensitivity formulation can be converted to a simple, parametric design sensitivity formulation.

In conventional shape design sensitivity analysis and optimization, the shape design parameter perturbs the boundary curve or surface [12]. Thus, theoretically it suffices that the shape design sensitivity formulation can be expressed in terms of the boundary functional. When the finite element method is used for a numerical approach, however, function evaluation on the boundary is not inherently accurate. Thus, the domain method has been developed in which the boundary perturbation induces the domain perturbation. However, the mapping from the boundary perturbation to the domain perturbation is not a one-to-one relation. Thus, various methods have been developed to calculate the domain design velocity field [12]. However, the proposed method eliminates this inconvenience because the formulation only affects the elements on the structural boundary. The numerical integration involved in the sensitivity calculation is limited to those elements on the boundary, which makes the proposed approach more efficient.

2. Eulerian representation of geometry

Conventional geometric representation and shape optimization of a solid structure is based on the Lagrangian approach, in which the structural domain and boundary are changed according to shape design parameters. Geometric details such as fillet surfaces and curvatures can be accurately represented in this approach. However, when a finite element-based numerical method is used to solve the shape optimization problem, mesh distortion is a major stumbling block for the Lagrangian approach. It is a difficult task to create a good quality mesh from a complicated CAD geometry (see Fig. 1(a)). Even if a regular mesh is initially created, the mesh quality deteriorates as the structural shape changes during the design optimization. In the Lagrangian approach, mesh adaptation and automatic re-meshing techniques are often used [13–15], which alleviate the numerical inaccuracies during shape optimization.

Recently, many researchers [5,6] began representing a structural domain using the Eulerian approach in which the grid is fixed in space. The region occupied by materials has a full shape density, while the void has zero shape density. The shape change can be characterized using an analogy of fluid flow. The shape density in one region moves to neighboring regions as the structural shape changes. After being integrated with an optimization algorithm, this approach yields the modern form of the topology design (see Fig. 1(b)). Although the topology design approach can provide a creative conceptual design, it is difficult to extract geometric information for complicated three-dimensional structures. In addition, it is complicated to physically interpret those regions with intermediate densities (a gray area) between full material and a void. However, the mesh distortion problem in the Lagrangian shape design can be resolved here, because mesh geometry is fixed throughout the whole design process.

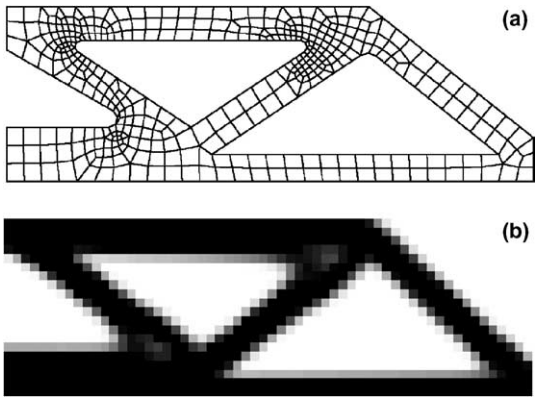

Fig. 1. Geometric representation methods. (a) Finite element mesh and (b) topology design.

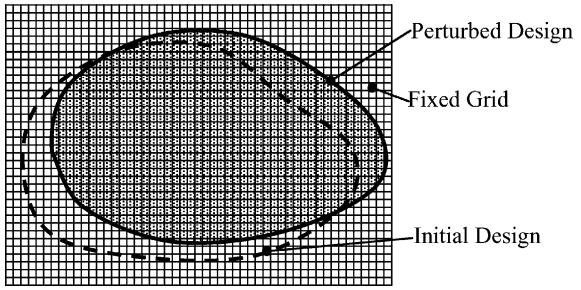

Fig. 2. Design change in the fixed grid. The perturbed design occupies new regions.

As has been discussed earlier, geometry-based shape parameterization has the advantage of accurately representing the structural domain, while the Eulerian approach has the advantage of resolving the mesh distortion problem. The proposed method uses geometry-based shape parameterization on the fixed grid (see Fig. 2). A solid geometry with domain Ω and boundary Γ is independently defined on a regular, rectangular mesh. If an element belongs to the domain Ω, then it has full shape density. If an element is outside domain Ω, then it has zero shape density.

Although the approximation in Fig. 2 seems straightforward, a technical difficulty exists for those elements that reside on the structural boundary. Part of the element belongs to the structural domain, while the other part is in a void. The idea of homogenization is used for the elements on the geometric boundary. The participation of each element can be determined using shape density, which measures the amount of element area that belongs to the structural domain Ω. Let the area of element m be A_m, and let the area that belongs to Ω be a_m. The shape density of element m can be calculated by

$$u_m = \begin{cases} 1, & \text{if } A_m \cap \Omega = A_m, \\ 0, & \text{if } A_m \cap \Omega = \emptyset, \\ a_m/A_m, & \text{if } A_m \in \Gamma, \end{cases} \tag{1}$$

where $A_m \cap \Omega = A_m$ represents the situation when element m belongs to the inside domain Ω (elements 2 and 3 in Fig. 3), while $A_m \cap \Omega = \emptyset$ represents the situation when no part of element m is located in Ω (elements 7, 8, and 9). When boundary Γ resides in the element (elements 1, 4, 5, and 6), the shape density u_m is the fraction of the area a_m that belongs to Ω.

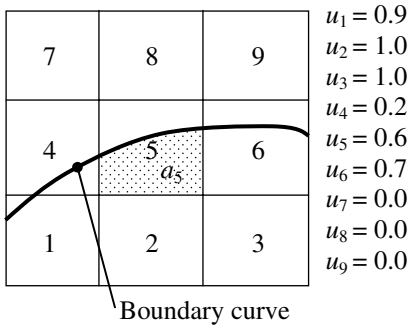

Fig. 3. Shape densities near the geometric boundary.

In order to calculate shape density u_m, domain integration is required for those elements on the geometric boundary. Since the boundary curve arbitrarily cuts through the element, it is difficult to set up a general domain integration procedure. Instead of integrating the area, Green's theorem [23] is employed to convert domain integration into boundary integration, which produces a more convenient expression. For example, for general two-dimensional problems area integration can be represented by

$$a_m = \int\int_{A_m \cap \Omega} \mathrm{d}\Omega = \int_C x_1 \, \mathrm{d}x_2, \tag{2}$$

where x_1 and x_2 are two coordinate directions and C is the curve that surrounds the area a_m in the counterclockwise direction. Curve C consists of straight element boundary lines and a geometric boundary curve. The integral in (2) that runs along the straight element boundary line is trivial since either x_1 or x_2 is constant. In the case of a boundary curve, it is assumed that parameter ξ is used to represent the curve, such that the expressions of $x_1(\xi)$ and $x_2(\xi)$ are available. Using the chain rule of differentiation, the integral in (2) can easily be converted to an integral with respect to parameter ξ. After calculating a_m, the shape density can be obtained from (1).

After determining the shape densities of boundary elements, the shape density of the interior or exterior can easily be determined using the following methods. First, it is assumed that the geometric boundary exists within the fixed finite element grid. Starting from the left-most element in a row, the shape density value is changed to either zero or one as it meets boundary elements, as illustrated in Fig. 4.

Alternatively, if the surface geometry information is available in addition to the curve geometry, then that information can be used to identify those elements that belong to the interior of the geometry. For example, when a parametric surface information $\mathbf{x}(\xi, \eta)$ is available, the interior elements can be found by incrementally searching parameters ξ and η.

During structural analysis, the material property of each element is augmented using the shape density, as

$$E_m = u_m E, \tag{3}$$

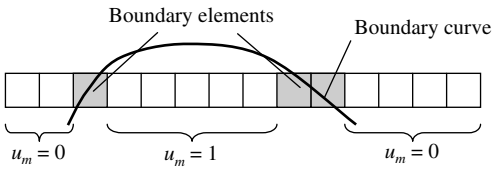

Fig. 4. Shape densities of elements in a row.

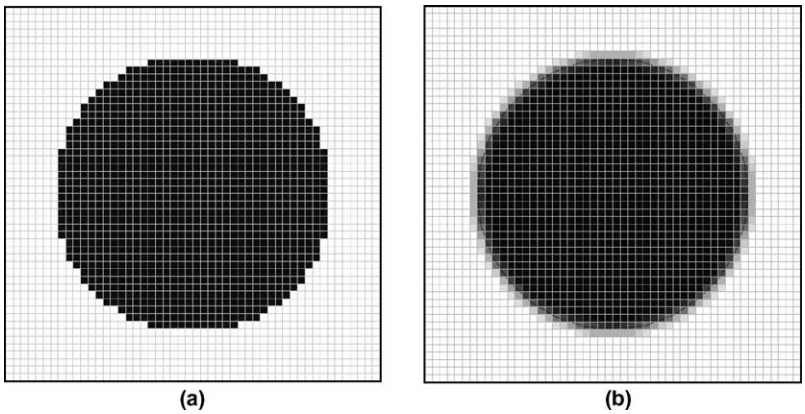

Fig. 5. Approximation of a circle using pixel and boundary homogenization. (a) Pixel approximation and (b) boundary homogenization.

where E is Young's modulus of the nominal material and E_m is the augmented modulus. Since Poisson's ratio is related to the lateral contraction during tensile deformation, it is fixed during this augmentation process. In practical application, the shape density for the void has a small value instead of zero in order to avoid numerical singularities during the finite element analysis procedure [6].

The approximation of domain Ω in Fig. 3 is different from the idea of pixels [16], in which a continuum structure is divided by a number of squares. In order to approximate the boundary reasonably, a very fine pixel mesh is required in the pixel-based approach. However, with the proposed method the effect of the continuous boundary is reflected by using boundary homogenization. As an example, in Fig. 5 a circle is approximated using pixel approximation and boundary homogenization. It is clear that the boundary homogenization method provides a smooth transition between structural and void parts. Indeed, the gray boundary of the topology design result in Fig. 1(b) should be understood in the same context as boundary homogenization. However, in the proposed method the structural domain is still represented using boundary curves and Fig. 5(b) is a mere approximation of the geometry.

3. Finite element analysis

The proposed Eulerian shape representation method has an advantage from the viewpoint of finite element analysis. Since all elements have an identical shape, it is very efficient to construct one element stiffness matrix and to use it repeatedly. Especially, when the element is square, the element stiffness matrix can be calculated analytically [17].

In the continuum domain, the weak form [18] of the structural problem can be written in the following form:

$$a_{\mathbf{u}}(\mathbf{z},\bar{\mathbf{z}}) = \ell_{\mathbf{u}}(\bar{\mathbf{z}}), \quad \forall \bar{\mathbf{z}} \in \mathbb{Z}, \tag{4}$$

where $\mathbb{Z}$ is the space of kinematically admissible displacements, and "$\forall \bar{\mathbf{z}} \in \mathbb{Z}$" means for all virtual displacements $\bar{\mathbf{z}}$ that belong to $\mathbb{Z}$. Eq. (4) is a variational equation with displacement $\mathbf{z}$ as a solution. In (4),

$$a_{\mathbf{u}}(\mathbf{z},\bar{\mathbf{z}}) = \int\int_{\Omega} \boldsymbol{\epsilon}(\bar{\mathbf{z}})^{\mathrm{T}} \mathbf{C} \boldsymbol{\epsilon}(\mathbf{z}) \, \mathrm{d}\Omega \tag{5}$$

and

$$\ell_{\mathbf{u}}(\bar{\mathbf{z}}) = \int\int_{\Omega} \bar{\mathbf{z}}^{\mathrm{T}}\mathbf{f}\,\mathrm{d}\Omega + \int_{\Gamma^s} \bar{\mathbf{z}}^{\mathrm{T}}\mathbf{T}\,\mathrm{d}\Gamma \tag{6}$$

are the structural bilinear and load linear forms, respectively. In (5), $\boldsymbol{\epsilon}(\mathbf{z})$ is the engineering strain vector, and $\mathbf{C}$ is the linear elastic constitutive matrix. In (6), $\mathbf{f}$ is the body force and $\mathbf{T}$ is the surface traction on the traction boundary Γ^s. The structural problem described in (4), with definitions in (5) and (6), is a standard form in the Lagrangian approach. In this case, Ω represents the structural domain.

With the Eulerian approach, Ω is the whole domain, including both the structure and void. Let the domain Ω be composed of NE sub-domains (finite elements), and let each sub-domain Ω_m have shape density u_m. Then, the structural bilinear and load linear forms can be written in the following forms:

$$a_{\mathbf{u}}(\mathbf{z},\bar{\mathbf{z}}) = \sum_{m=1}^{NE} \int\int_{\Omega_m} \boldsymbol{\epsilon}(\bar{\mathbf{z}})^{\mathrm{T}}\mathbf{C}\boldsymbol{\epsilon}(\mathbf{z})u_m\,\mathrm{d}\Omega_m \tag{7}$$

and

$$\ell_{\mathbf{u}}(\bar{\mathbf{z}}) = \sum_{m=1}^{NE} \left(\int\int_{\Omega_m} \bar{\mathbf{z}}^{\mathrm{T}}\mathbf{f}u_m\,\mathrm{d}\Omega \right) + \int_{\Gamma^s} \bar{\mathbf{z}}^{\mathrm{T}}\mathbf{T}\,\mathrm{d}\Gamma, \tag{8}$$

where in the definitions of $a_{\mathbf{u}}(\bullet,\bullet)$ and $\ell_{\mathbf{u}}(\bullet)$, the index $\mathbf{u}$ is used to denote the dependence of these forms on the design variable vector $\mathbf{u} = [u_1, u_2, \ldots, u_{NE}]^{\mathrm{T}}$. Since u_m is constant within the element, it can be taken outside the integral. It is assumed that the traction force is independent of the design. Even if the domain decomposition has been introduced in (7) and (8), all variables are still in the continuum level.

In the Lagrangian approach, there exists a discrete set of nodes along the geometric boundary. Thus, the displacement boundary condition can be applied to those nodes on the boundary. In the Eulerian approach, since the geometry moves around within a fixed set of finite elements, it is better to apply the displacement boundary condition on the geometric curve or point. However, the geometric boundary is often located in the interior of the boundary elements. Thus, it is not trivial to apply the displacement boundary conditions along the geometric curve. As an approximation, one can fix all elements that intersect with the displacement boundary curve (see Fig. 6). However, this method overestimates the effect of boundary conditions.

Recently, Clark and Anderson [19] proposed the penalty boundary method, which can impose the essential and natural boundary conditions when the geometry and finite elements are not conforming. Let Γ^h be the essential boundary of the structure in which the displacement is prescribed. In the penalty boundary method, the prescribed boundary condition is imposed approximately by using the penalty function, as

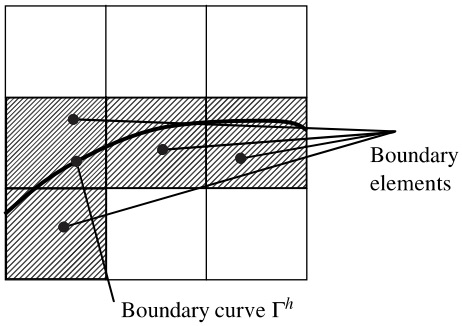

Fig. 6. Displacement boundary conditions on the boundary elements.

$$P(\mathbf{z}) = \frac{1}{2}\alpha \int_{\Gamma^h} (\mathbf{z}-\mathbf{g})^{\mathrm{T}}(\mathbf{z}-\mathbf{g})\,\mathrm{d}\Gamma, \tag{9}$$

where $\mathbf{g}$ is the prescribed displacement (usually zero for linear elastic problems), and α is the penalty parameter. If the displacement $\mathbf{z}$ on the boundary Γ^h is different from the given value, then (9) penalizes the structural potential energy. In order to incorporate (9) with the weak form of the structural problem, the variation of the penalty function needs to be obtained, as

$$\overline{P}(\mathbf{z},\bar{\mathbf{z}}) = \alpha \int_{\Gamma^h} \bar{\mathbf{z}}^{\mathrm{T}}(\mathbf{z}-\mathbf{g})\,\mathrm{d}\Gamma, \tag{10}$$

where the superposed "$-$" denotes the variation of the function. This variation needs to be added to the weak form in (4). A similar approach to the discrete model has been taken by Belytschko et al. [20] when they impose the essential boundary condition on the meshfree formulation. They imposed the penalty method because the meshfree interpolation function did not satisfy the Dirac-delta property. When the finite element method is used, a discrete version of (10) needs to be developed. Let the boundary Γ^h intersect with element m. Then, the approximation of (10) becomes

$$P(\mathbf{z},\bar{\mathbf{z}}) = \bar{\mathbf{d}}^{\mathrm{T}}\left[\alpha \int_{\Gamma^h\cap\Omega_m} \mathbf{N}^{\mathrm{T}}\mathbf{N}\,\mathrm{d}\Gamma\right]\mathbf{d} - \bar{\mathbf{d}}^{\mathrm{T}}\left[\alpha \int_{\Gamma^h\cap\Omega_m} \mathbf{N}^{\mathrm{T}}\mathbf{g}\,\mathrm{d}\Gamma\right], \tag{11}$$

where $\mathbf{N}$ is the matrix of shape functions using Lagrange interpolation, $\mathbf{d}$ is the vector of nodal displacements, and $\bar{\mathbf{d}}$ is the vector of virtual displacements. Note that the integration only performs along $\Gamma^h \cap \Omega_m$.

The same approach can be applied to the natural boundary condition in which the traction force is applied along the boundary curve. However, in such a case the derivation of the penalty term involves more mathematical elaborations. The penalty function for the traction boundary condition can be stated as

$$Q(\mathbf{z}) = \frac{1}{2}\alpha \int_{\Gamma^s} [\boldsymbol{\sigma}(\mathbf{z})\mathbf{n} - \mathbf{T}]^{\mathrm{T}}[\boldsymbol{\sigma}(\mathbf{z})\mathbf{n} - \mathbf{T}]\,\mathrm{d}\Gamma, \tag{12}$$

where $\mathbf{n}$ is the unit outward normal vector to the boundary and $\boldsymbol{\sigma}(\mathbf{z})$ is the stress matrix. In the small deformation problem, the normal vector is calculated based on the initial geometry. Thus, stress is the only function of displacement in (12). The penalty parameter α in (12) can be different from that in (9). Similarly to the displacement penalty function, the variation of $Q(\mathbf{z})$ can be taken as

$$\overline{Q}(\mathbf{z},\bar{\mathbf{z}}) = \alpha \int_{\Gamma^s} [\boldsymbol{\sigma}(\bar{\mathbf{z}})\mathbf{n}]^{\mathrm{T}}[\boldsymbol{\sigma}(\mathbf{z})\mathbf{n} - \mathbf{T}]\,\mathrm{d}\Gamma. \tag{13}$$

This variation needs to be added to the weak form in (4). In conjunction with the finite element method, the variation in (13) can be approximated by

$$\overline{Q}(\mathbf{z},\bar{\mathbf{z}}) = \bar{\mathbf{d}}^{\mathrm{T}}\left[\alpha \int_{\Gamma^s\cap\Omega_m} \mathbf{B}^{\mathrm{T}}\mathbf{C}^{\mathrm{T}}\mathbf{S}^{\mathrm{T}}\mathbf{S}\mathbf{C}\mathbf{B}\,\mathrm{d}\Gamma\right]\mathbf{d} - \bar{\mathbf{d}}^{\mathrm{T}}\left[\alpha \int_{\Gamma^s\cap\Omega_m} \mathbf{B}^{\mathrm{T}}\mathbf{C}^{\mathrm{T}}\mathbf{S}^{\mathrm{T}}\mathbf{T}\,\mathrm{d}\Gamma\right], \tag{14}$$

where $\mathbf{B}$ is the displacement-strain relation matrix, $\mathbf{C}$ is the elasticity matrix, $\mathbf{S}$ is the matrix of normal vectors. In two-dimensional plane stress problem with the $a \times a$ square finite element, these three matrices are defined as

$$\mathbf{B} = \begin{bmatrix} y-a & 0 & -y+a & 0 & y & 0 & -y & 0 \\ 0 & x-a & 0 & -x & 0 & x & 0 & -x+a \\ x-a & y-a & -x & -y+a & x & y & -x+a & -y \end{bmatrix}, \tag{15}$$

$$\mathbf{C} = \frac{E}{1-v^2}\begin{bmatrix} 1 & v & 0 \\ v & 1 & 0 \\ 0 & 0 & \dfrac{1-v}{2} \end{bmatrix}, \tag{16}$$

and

$$\mathbf{S} = \begin{bmatrix} n_x & 0 & n_y \\ 0 & n_y & n_x \end{bmatrix}. \tag{17}$$

Note that the integration in (14) only performs along $\Gamma^s \cap \Omega_m$.

For two-dimensional finite elements with square shape, the stiffness matrix can be calculated analytically [17] as

$$[\mathbf{k}] = \frac{E}{1-v^2}\begin{bmatrix}
\dfrac{3-v}{6} & \dfrac{1+v}{8} & -\dfrac{3-v}{12} & \dfrac{-1+3v}{8} & \dfrac{-3+v}{12} & -\dfrac{1+v}{8} & \dfrac{v}{6} & \dfrac{1-3v}{8} \\
\dfrac{1+v}{8} & \dfrac{3-v}{6} & \dfrac{1-3v}{8} & \dfrac{v}{6} & -\dfrac{1+v}{8} & \dfrac{-3+v}{12} & \dfrac{-1+3v}{8} & -\dfrac{3-v}{12} \\
-\dfrac{3-v}{12} & \dfrac{1-3v}{8} & \dfrac{3-v}{6} & -\dfrac{1+v}{8} & \dfrac{v}{6} & \dfrac{-1+3v}{8} & \dfrac{-3+v}{12} & \dfrac{1+v}{8} \\
\dfrac{-1+3v}{8} & \dfrac{v}{6} & -\dfrac{1+v}{8} & \dfrac{3-v}{6} & \dfrac{1-3v}{8} & -\dfrac{3-v}{12} & \dfrac{1+v}{8} & \dfrac{-3+v}{12} \\
\dfrac{-3+v}{12} & -\dfrac{1+v}{8} & \dfrac{v}{6} & \dfrac{1-3v}{8} & \dfrac{3-v}{6} & \dfrac{1+v}{8} & -\dfrac{3-v}{12} & \dfrac{-1+3v}{8} \\
-\dfrac{1+v}{8} & \dfrac{-3+v}{12} & \dfrac{-1+3v}{8} & -\dfrac{3-v}{12} & \dfrac{1+v}{8} & \dfrac{3-v}{6} & \dfrac{1-3v}{8} & \dfrac{v}{6} \\
\dfrac{v}{6} & \dfrac{-1+3v}{8} & \dfrac{-3+v}{12} & \dfrac{1+v}{8} & -\dfrac{3-v}{12} & \dfrac{1-3v}{8} & \dfrac{3-v}{6} & -\dfrac{1+v}{8} \\
\dfrac{1-3v}{8} & -\dfrac{3-v}{12} & \dfrac{1+v}{8} & \dfrac{-3+v}{12} & \dfrac{-1+3v}{8} & \dfrac{v}{6} & -\dfrac{1+v}{8} & \dfrac{3-v}{6}
\end{bmatrix}. \tag{18}$$

Note that the stiffness matrix [**k**] is not a function of geometry, but a function of material properties. In fact, it is independent of element size. Since all elements have the same [**k**] matrix with different shape density, the element stiffness matrix can be calculated by

$$[\mathbf{k}_m] = \left[u_m \mathbf{k} + \alpha \int_{\Gamma^h \cap \Omega_m} \mathbf{N}^{\mathrm{T}}\mathbf{N}\,\mathrm{d}\Gamma + \alpha \int_{\Gamma^s \cap \Omega_m} \mathbf{B}^{\mathrm{T}}\mathbf{C}^{\mathrm{T}}\mathbf{S}^{\mathrm{T}}\mathbf{S}\mathbf{C}\mathbf{B}\,\mathrm{d}\Gamma\right], \tag{19}$$

where the second part on the right-hand side is the contribution from the penalty displacement boundary method. It is only applied to those elements that reside on the essential boundaries. The third part is the contribution from the traction force. The applied force vector for the element can also be calculated by

$$\{\mathbf{f}_m\} = u_m \int\int_{\Omega_m} \mathbf{N}^{\mathrm{T}}\mathbf{f}\,\mathrm{d}\Omega + \alpha \int_{\Gamma^h \cap \Omega_m} \mathbf{N}^{\mathrm{T}}\mathbf{g}\,\mathrm{d}\Gamma + \alpha \int_{\Gamma^s \cap \Omega_m} \mathbf{B}^{\mathrm{T}}\mathbf{C}^{\mathrm{T}}\mathbf{S}^{\mathrm{T}}\mathbf{T}\,\mathrm{d}\Gamma, \tag{20}$$

where the second term of the right-hand side is the contribution from the penalty boundary method. In most linear static problems, the prescribed displacement is zero, i.e., $\mathbf{g} = \mathbf{0}$. In such a case, the penalty contribution vanishes. The element stiffness matrix and force vector are assembled to construct the global system of matrix equations as

$$[\mathbf{K}]\{\mathbf{D}\} = \{\mathbf{F}\}. \tag{21}$$

The theoretical aspect of the penalty boundary method is that the virtual displacement does not have to belong to the space of kinematically admissible displacements. The numerical aspect of the method is that the coefficient matrix can be ill-conditioned as the magnitude of the penalty parameter increases. Thus, there exists a possible difficulty when an iterative matrix solver is used.

Even if the proposed method has many attractive features from design and simulation points of view, it requires a numerically intensive procedure due to the larger number of finite elements in high resolution. For example, the torque arm structure in Section 6 has about 37,000 degrees-of-freedom even if it is a simple, two-dimensional example. It would be very expensive to store the global stiffness matrix in the computer memory. In this paper, a multi-frontal sparse matrix solver in the literature [21] is employed to store only non-zero components of the global stiffness matrix and to solve the finite element matrix equations.

4. Design parameterization

A major difference between the proposed method and topology design methods exists in the design parameterization process. In topology optimization, a design engineer does not have any freedom to control the design direction. The optimum shape (or topology) of the structure is determined by finding the shape density of individual elements, which does not guarantee any continuity or smoothness of the boundary unless a specific constraint is imposed. In the proposed method, design parameterization is similar to the conventional shape design problem in which the structural boundary changes according to the design velocity field. As will be shown later, it is unnecessary to define the domain design velocity field in the proposed method; the boundary design velocity field is enough to calculate design sensitivity information.

In the shape design problem, the parameters that determine the boundary curve are chosen as design variables. For example, when spline curves are used to represent the boundary, the location of control points can be chosen as design variables (an example will be shown in Section 6.1). As a design variable changes, the structural boundary and domain change continuously. Let the initial boundary Γ and domain Ω change to the perturbed boundary Γ_τ and domain Ω_τ, respectively. Such a shape perturbation process is analogous to the dynamic process, in which τ plays the role of time [22]. At the initial time $\tau = 0$, the structural domain is Ω and the boundary is Γ. When the first-order perturbation is used, the material point $\mathbf{x}_\tau$ can be denoted by

$$\mathbf{x}_\tau = \mathbf{x} + \tau \mathbf{V}(\mathbf{x}), \quad \mathbf{x} \in \Omega, \tag{22}$$

where $\mathbf{V}(\mathbf{x})$ is the design velocity field that designates the direction of shape change, and τ is a scalar parameter that controls the amount of shape change.

Eq. (22) describes the shape perturbation of the continuum model. If a discrete model follows the same perturbation as (22), then it is referred to in this paper as the Lagrangian approach. As with the continuum model, the initial shape of each finite element geometry changes according to the design velocity field, which frequently results in the mesh distortion problem. However, with the Eulerian approach, the discrete finite element model is fixed during the design perturbation (see Fig. 7), and each element has a shape density value between zero and one, based on the location. The effect of shape change is apparent through the shape density change. Moreover, this effect is only apparent for those elements on the structural boundary.

An important theoretical issue is how to interpret shape perturbation as a shape density change on the boundary. Note that shape perturbation is given as a vector quantity (design velocity field), but that shape density variation is a scalar quantity. As the structural shape changes in the direction of the design velocity field (Fig. 7), u_m of those elements on the boundary curve changes accordingly. By using standard variational formulas [22], the change of u_m can be denoted by

$$u_{m_\tau} = u_m + \tau \delta u_m, \tag{23}$$

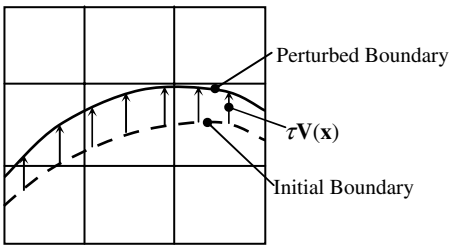

Fig. 7. Shape design perturbation and corresponding change of shape density.

where δu_m is the variation of the shape density. For those elements that reside within the structural domain, δu_m is zero. Thus, perturbation in (23) is only applied to those elements on the structural boundary.

As is clear from Fig. 7, when the boundary curve is perturbed in the direction of design velocity $\mathbf{V}(\mathbf{x})$, the shape density u_m is also changed. Attention is focused on element m, which resides on the boundary curve. The shape density at the perturbed design can be defined as

$$u_{m_\tau} = \frac{1}{A_m}\int\int_{A_m\cap\Omega_\tau} \mathrm{d}\Omega_\tau = \frac{1}{A_m}\int\int_{A_m\cap\Omega} |\mathbf{J}|\,\mathrm{d}\Omega, \tag{24}$$

where $\mathbf{J}$ is the Jacobian matrix of shape perturbation in (22), defined as

$$\mathbf{J} = \frac{\partial \mathbf{x}_\tau}{\partial \mathbf{x}} = \mathbf{I} + \tau\frac{\partial \mathbf{V}}{\partial \mathbf{x}}. \tag{25}$$

The material derivative formulas for the Jacobian can be found in Choi and Haug [22]. For example, the material derivative of the Jacobian becomes

$$\frac{\mathrm{d}}{\mathrm{d}\tau}|\mathbf{J}|\bigg|_{\tau=0} = \mathrm{div}\mathbf{V}, \tag{26}$$

where $\mathrm{div}\,\mathbf{V}$ is the divergence of the design velocity.

If the shape density in (24) is differentiated by τ, by using the formula in (26), then the relation between $\mathbf{V}(\mathbf{x})$ and δu_m can be obtained as

$$\delta u_m = \frac{1}{A_m}\int\int_{A_m\cap\Omega} \mathrm{div}\,\mathbf{V}\,\mathrm{d}\Omega = \frac{1}{A_m}\int_C \mathbf{V}^{\mathrm{T}}\mathbf{n}\,\mathrm{d}\Gamma, \tag{27}$$

where $\mathbf{n}$ is the outward unit normal vector to the boundary, and C is the boundary of area a_m moving in the counter-clockwise direction. The second equality in the above equation can be obtained from the divergence theorem [23]. It is interesting and important to note that only the normal component of the boundary velocity appears in (27) because the tangential component does not contribute to the shape change.

After design parameterization is completed, the corresponding design velocity $\mathbf{V}(\mathbf{x})$ is calculated on the boundary curve. For those elements on the boundary, the variation of shape density can be calculated by integrating the design velocity along the boundary curve.

In the Lagrangian approach, the only limitation of shape design parameterization is that it must maintain the topology of the structure. For example, the diameter of a hole in the plate cannot be greater than the dimension of the plate. In the Eulerian approach, there exists an additional limitation in design parameterization. As can be seen in Fig. 2, the structural boundary, which is used for design parameters, must stay within the fixed grid. In other words, the total design space occupied by the fixed grid must cover all possible design combinations. In practice, the size of the fixed grid can be chosen based on the upper and lower bounds of the design parameters.

5. Design sensitivity analysis

The purpose of design sensitivity analysis is to develop relationships between a variation in shape and resulting variations in functionals that arise in shape design problems. For demonstration purposes, a linear elastic problem is considered in the following sensitivity development. However, a general nonlinear problem can also be taken into account using a similar approach.

5.1. Direct differentiation method

In this section, design parameterization from the previous section is utilized to derive the shape sensitivity expression in terms of δu_m. Displacement $\mathbf{z}$ in (4) implicitly depends on the design through the structural problem in (4), which must be calculated from the design sensitivity equation, as explained below. An important component of design sensitivity analysis is calculating the variation of the state variable (in this case, displacement $\mathbf{z}$) by differentiating (4) with respect to the design, or equivalently, τ. To that end, we define the variation of the state variable, as

$$\mathbf{z}' \equiv \frac{\mathrm{d}}{\mathrm{d}\tau}\mathbf{z}(\mathbf{x};\mathbf{u}+\tau\delta\mathbf{u})\bigg|_{\tau=0} = \mathbf{z}\frac{\partial \mathbf{z}}{\partial \mathbf{u}}\bigg|_{\tau=0}\cdot\delta\mathbf{u}. \tag{28}$$

Note that $\mathbf{z}'$ depends on the design $\mathbf{u}$, where the variation is evaluated, and on the direction $\delta\mathbf{u}$ of the design variation. The goal of the direct differentiation method is to calculate $\mathbf{z}'$ first, and then using the chain rule of differentiation to calculate the sensitivity of performance functions.

Similarly to (28), the structural bilinear and load linear forms can be differentiated with respect to the design. Although the design vector and its variation contain NE components, only boundary elements need to be considered in the calculation of δu_m because it is zero for those elements inside or outside the structural domain. Let M be the number of elements that belong to the structural boundary. The variation of the structural bilinear form can be obtained using the chain rule of differentiation, as

$$\frac{\mathrm{d}}{\mathrm{d}\tau}\left[a_{\mathbf{u}+\tau\delta\mathbf{u}}(\mathbf{z}(\mathbf{x};\mathbf{u}+\tau\delta\mathbf{u}),\bar{\mathbf{z}})\right]\bigg|_{\tau=0} = a'_{\delta\mathbf{u}}(\mathbf{z},\bar{\mathbf{z}}) + a_{\mathbf{u}}(\mathbf{z}',\bar{\mathbf{z}}), \tag{29}$$

where

$$a'_{\delta\mathbf{u}}(\mathbf{z},\bar{\mathbf{z}}) = \sum_{m=1}^{M}\int\int_{\Omega_m}\boldsymbol{\epsilon}(\bar{\mathbf{z}})^{\mathrm{T}}\mathbf{C}\boldsymbol{\epsilon}(\mathbf{z})\,\mathrm{d}\Omega\,\delta u_m \tag{30}$$

is the dependence of the bilinear form on the design. If the structural problem in (4) is solved for $\mathbf{z}$ and the design variation δu_m in (27) is available as a result of design parameterization, then $a'_{\delta\mathbf{u}}(\mathbf{z},\bar{\mathbf{z}})$ can be readily calculated by following the same integration procedure used in finite element analysis. The second term on the right-hand side of (29) is the same as the bilinear form in (7) if displacement $\mathbf{z}$ is replaced by $\mathbf{z}'$, which will be solved.

The variation of the load linear form can also be obtained by following a similar procedure

$$\frac{\mathrm{d}}{\mathrm{d}\tau}\ell_{\mathbf{u}+\tau\delta\mathbf{u}}(\bar{\mathbf{z}})\bigg|_{\tau=0} = \ell'_{\delta\mathbf{u}}(\bar{\mathbf{z}}) = \sum_{m=1}^{M}\int\int_{\Omega_m}\bar{\mathbf{z}}^{\mathrm{T}}\mathbf{f}\,\mathrm{d}\Omega\,\delta u_m. \tag{31}$$

When the traction boundary is changed according to the design, careful treatment is required regarding boundary homogenization, which is not developed in this paper. When a concentrated load is applied to the structure, the variation of the load linear form in (31) vanishes because the load is independent of the design.

After differentiating (4) at the perturbed design and using the formulas in (29) and (31), the following *design sensitivity equation* can be obtained:

$$a_{\mathbf{u}}(\mathbf{z}', \bar{\mathbf{z}}) = \ell'_{\delta\mathbf{u}}(\bar{\mathbf{z}}) - a'_{\delta\mathbf{u}}(\mathbf{z}, \bar{\mathbf{z}}), \quad \forall \bar{\mathbf{z}} \in \mathbb{Z}, \tag{32}$$

where the solution $\mathbf{z}'$ is desired. If the right-hand side is considered to be an applied load, Eq. (32) is similar to the structural problem in (4) with a different load, which is called the *fictitious load*. When a design variable is defined, the corresponding design velocity $\mathbf{V}(\mathbf{x})$ can be calculated on the structural boundary. Using this design velocity, the design variation δu_m can be calculated from (27).

By following the same discretization as the finite element method, the matrix equation for the design sensitivity problem (32) can be obtained as

$$[\mathbf{K}]\{\mathbf{D}'\} = \{\mathbf{F}^{\text{fic}}\}, \tag{33}$$

where $\{\mathbf{D}'\}$ is the sensitivity of the nodal displacement vector and $\{\mathbf{F}^{\text{fic}}\}$ is the fictitious load vector, defined as

$$\{\mathbf{F}^{\text{fic}}\} = \sum_{m=1}^{M} \int\int_{\Omega_m} \mathbf{N}^{\mathrm{T}}\mathbf{f}\delta u_m \,\mathrm{d}\Omega - \sum_{m=1}^{M} \int\int_{\Omega_m} \mathbf{B}^{\mathrm{T}}\mathbf{C}\mathbf{B}\mathbf{d}\delta u_m \,\mathrm{d}\Omega. \tag{34}$$

All information in (34) is already available from the structural analysis. Thus, calculating the integrals in (34) is relatively convenient with the design variation δu_m.

Consider a general performance function defined in terms of integral over the domain Ω, as

$$\psi(\mathbf{u}, \mathbf{z}(\mathbf{u})) = \int\int_{\Omega} b(\mathbf{u}, \mathbf{z}(\mathbf{u}))\,\mathrm{d}\Omega. \tag{35}$$

The performance ψ can be a point-wise function if the Dirac-delta measure is used as an integrand. If the structural volume or area is a performance function, then the shape density u_m can be an integrand with summation over all elements. If stress at element m is involved, then the integrand is the stress function and integrated over sub-domain Ω_m. The sensitivity of ψ in (35) can be obtained by taking variation with respect to the design $\mathbf{u}$, as

$$\psi' = \int\int_{\Omega} \left[\frac{\partial b^{\mathrm{T}}}{\partial \mathbf{u}}\,\delta\mathbf{u} + \frac{\partial b^{\mathrm{T}}}{\partial \mathbf{z}}\,\mathbf{z}'\right]\mathrm{d}\Omega. \tag{36}$$

Eq. (36) can be readily evaluated using the solution of (32) and δu_m. The gradient information that is necessary for design optimization is equivalent to the coefficient of $\delta\mathbf{u}$. Thus, the coefficient of $\delta\mathbf{u}$ in (36) is called the *sensitivity coefficient*.

Compared to the shape design sensitivity formulation in the Lagrangian approach, the expressions in (30) and (31) provide significantly simple computational methods, since their expressions also appear during regular finite element analysis. In geometry-based shape optimization, domain integration is involved in (30) and (31). However, only the boundary integral is sufficient for the proposed method.

From the computational viewpoint, the left-hand side of (33) is the same as that of (21) if $\{\mathbf{D}'\}$ is replaced by $\{\mathbf{D}\}$. Thus, solving the sensitivity equation becomes very efficient when a direct matrix solver is used. For example, the coefficient matrix $[K]$ in (21) is factorized during the finite element analysis. In design sensitivity analysis, the factorized coefficient matrix can be used for the calculation of $\mathbf{z}'$. Thus, the major computational effort involved in sensitivity analysis is to construct the fictitious load in (34) and then forward- and backward-substitutions to solve for $\mathbf{z}'$.

5.2. Adjoint variable method

The main idea of the adjoint variable method is to avoid the direct calculation of $\mathbf{z}'$ in (32). Since the sensitivity expression in (36) requires the calculation of $\mathbf{z}'$, the adjoint problem is defined using the coefficient of $\mathbf{z}'$ in (36) as a load term. Accordingly, the *adjoint problem* is defined as

$$a_{\mathbf{u}}(\boldsymbol{\lambda}, \bar{\boldsymbol{\lambda}}) = \int\int_{\Omega} \left[\frac{\partial b}{\partial \mathbf{z}}^{\mathrm{T}} \bar{\boldsymbol{\lambda}}\right] \mathrm{d}\Omega, \quad \forall \bar{\boldsymbol{\lambda}} \in \mathbb{Z}, \tag{37}$$

where the *adjoint solution* $\boldsymbol{\lambda}$ is unknown and its variation $\bar{\boldsymbol{\lambda}}$ plays the same role as $\bar{\mathbf{z}}$ in (4). By replacing $\bar{\boldsymbol{\lambda}}$ with $\mathbf{z}'$ in (37) and by replacing $\bar{\mathbf{z}}$ with $\boldsymbol{\lambda}$ in (32), it can be shown that the second integrand of (36) can be represented by

$$\int\int_{\Omega} \left[\frac{\partial b}{\partial \mathbf{z}}^{\mathrm{T}} \mathbf{z}'\right] \mathrm{d}\Omega = \ell'_{\delta\mathbf{u}}(\lambda) - a'_{\delta\mathbf{u}}(\mathbf{z}, \lambda). \tag{38}$$

In deriving the above equation, the symmetric property of the energy bilinear form $a_{\mathbf{u}}(\bullet, \bullet)$ has been used. The physical meaning of (38) is that the implicit dependence of the performance function has been eliminated using the adjoint solution. Thus, the sensitivity of the performance function can be expressed in terms of the structural solution $\mathbf{z}$ and the adjoint solution $\boldsymbol{\lambda}$ as

$$\psi' = \int\int_{\Omega} \left[\frac{\partial b}{\partial \mathbf{u}}^{\mathrm{T}} \delta\mathbf{u}\right] \mathrm{d}\Omega + \ell'_{\delta\mathbf{u}}(\lambda) - a'_{\delta\mathbf{u}}(\mathbf{z}, \boldsymbol{\lambda}). \tag{39}$$

It would be beneficial to compare the efficiency of the direct differentiation and adjoint variable methods from the computational viewpoint. It is interesting to note that the adjoint equation (37) is independent of the design. In fact, each performance function has a different adjoint load on the right-hand side. Thus, Eq. (37) needs to be solved per each performance function. In the direct differentiation method in (32), however, the sensitivity equation needs to be solved per each design variable. Thus, the adjoint method is more efficient when the number of performance measures is smaller than the number of design variables, which is the case for most optimization problems.

In the numerical approach, the adjoint problem in (37) needs to be discretized using the same method as in structural analysis. The matrix equation for the adjoint problem becomes

$$[\mathbf{K}]\{\boldsymbol{\Lambda}\} = \{\mathbf{F}^{\mathrm{adj}}\}, \tag{40}$$

where $\{\boldsymbol{\Lambda}\}$ is the nodal solution of the global adjoint vector and $\{\mathbf{F}^{\mathrm{adj}}\}$ is the adjoint load vector, defined by

$$\{\mathbf{F}^{\mathrm{adj}}\} = \int\int_{\Omega} \frac{\partial b}{\partial \mathbf{z}} \mathrm{d}\Omega. \tag{41}$$

The calculation of sensitivity in (39) involves a similar procedure to the fictitious load in (34). This process must be repeated for each design variable, because the fictitious load depends on the design.

6. Numerical example

In this section, a numerical example is presented in order to compare it with the shape optimization results in the literature [4,24].

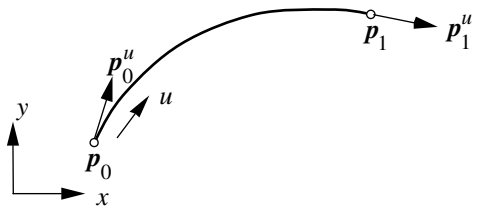

Fig. 8. Spline curve that represents the structural boundary.

6.1. Computational geometry

Many methods are available in representing the boundary geometry of the structure. Although the proposed Eulerian representation method can be applied to general methods, let us consider a particular example using geometric curves, as shown in Fig. 8. In the geometric curve, the coordinates of the curve are represented using a parameter $\xi \in [0, 1]$ as

$$\mathbf{x}(\xi) = [\mathbf{p}_0, \mathbf{p}_1, \mathbf{p}_0^{\xi}, \mathbf{p}_1^{\xi}] \begin{bmatrix} 2 & -3 & 0 & 1 \\ -2 & 3 & 0 & 0 \\ 1 & -2 & 1 & 0 \\ 1 & -1 & 0 & 0 \end{bmatrix} \begin{bmatrix} \xi^3 \\ \xi^2 \\ \xi \\ 1 \end{bmatrix}, \tag{42}$$

$$\equiv [\mathbf{G}][\mathbf{M}][\boldsymbol{\xi}],$$

where $\mathbf{p}_0 = [p_x, p_y]^{\mathrm{T}}_{\xi=0}$ and $\mathbf{p}_1 = [p_x, p_y]^{\mathrm{T}}_{\xi=1}$ are locations of two end points, respectively, and $\mathbf{p}_0^{\xi} = [\mathrm{d}p_x/\mathrm{d}\xi, \mathrm{d}p_y/\mathrm{d}\xi]^{\mathrm{T}}_{\xi=0}$ and $\mathbf{p}_1^{\xi} = [\mathrm{d}p_x/\mathrm{d}\xi, \mathrm{d}p_y/\mathrm{d}\xi]^{\mathrm{T}}_{\xi=1}$ are tangent vectors at both points, respectively.

Design variables for the shape problem can be defined by choosing a component of the matrix [**G**]. For example, when a design variable moves point $\mathbf{p}_0$ in the x-direction, we can define a unit perturbation matrix by

$$[\mathbf{B}] = \begin{bmatrix} 1 & 0 & 0 & 0 \\ 0 & 0 & 0 & 0 \end{bmatrix}. \tag{43}$$

Then, the design velocity vector can be defined by replacing matrix [**G**] with matrix [**B**], as

$$\mathbf{V}(\xi) = [\mathbf{B}][\mathbf{M}][\boldsymbol{\xi}], \tag{44}$$

where the matrix [**B**] is a unit perturbation of the matrix [G] in the direction of the design variable. The tangent vector and normal vector to the boundary can be calculated by differentiating (42) with respect to parameter ξ.

6.2. Torque arm model

A design optimization of the torque arm model has been demonstrated by many different approaches. Bennett and Botkin [4] used the Lagrangian method with parametric boundary geometry. Kim et al. [24] used the meshfree method to optimize the shape of the torque arm. Jang et al. [25] performed the design optimization of the torque arm model using the multi-scale wavelet approach that can locally improve the resolution of the solution accuracy. This model is considered as a benchmark problem in shape optimization. The torque arm model shown in Fig. 9 is composed of 32 points, 28 boundary curves, and 16 surfaces. A rectangular domain is established with the lower-left corner being $(-7, -8)$ and the upper-right

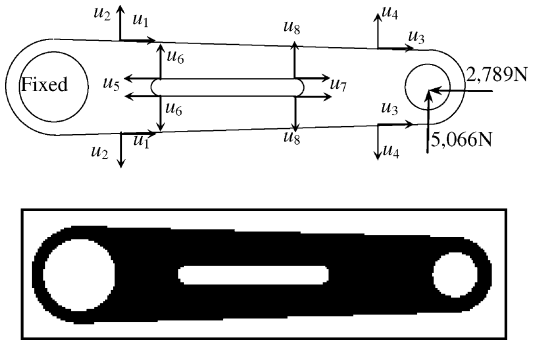

Fig. 9. Design parameterization and boundary homogenization of the torque arm with pixel size = 0.21 cm.

corner being (49, 8), which covers the whole structure. A 0.21 cm × 0.21 cm square is used to discretize the rectangular domain so that the whole domain is approximated by a 267×77 grid. Fig. 9 also shows the structural domain that is identified using the boundary homogenization method. The black interior domain has a full shape density ($u = 1.0$), while the gray boundary represents the intermediate shape density ($0 < u < 1$) calculated using (1). All void areas are represented in white. For material properties, the following values are used: Young's modulus = 207.4 GPa, Poisson's ratio = 0.3, and thickness = 0.3 cm.

In finite element analysis, the left circle is fixed and the horizontal and vertical forces are applied at the center of the right circle. In order to apply for the displacement boundary conditions, the boundary curves that correspond to the left circle are identified first. It is trivial to retrieve boundary element information corresponding to the displacement boundary curves. Then, the penalty boundary method explained in Section 3 is used to impose the displacement boundary condition. Thus, in this approach displacement boundary conditions are applied in a layer of elements. The penalty parameter for applying the boundary conditions is one hundred times greater than Young's modulus. The force boundary condition can also be applied in the same manner.

A maximum stress of about 248 MPa appears at the top and bottom surfaces of the torque arm (see Fig. 10). This result is expected because the applied force is a superposition of compressive and bending loads. In addition, a relatively high stress concentration is observed at the end of the interior slot, which is caused by distortion at the small radius region.

From the mathematical point of view, the pixel-based geometric representation may cause singularity at the non-smooth boundary, which is inevitable when the inclined boundary is approximated by x- and y-directional squares. However, the proposed approach reduces such singularity by gradually reducing the shape density at the boundary. However, different material properties between interior and boundary elements cause stress discontinuity. A smoothening algorithm in stress may help to reduce discontinuity. For detailed discussion, refer to García and Steven [7], Jang et al. [25] and Duysinx and Bendsøe [26].

Since design parameters are defined on the geometric model, the horizontal and vertical movements of geometric points can be selected as design parameters. Eight design parameters are chosen that can change

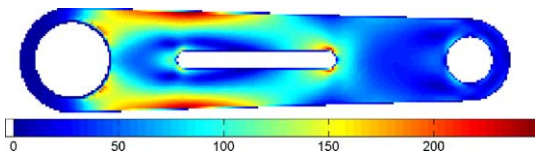

Fig. 10. Finite element analysis results of the torque arm (equivalent stress plot). Unit: MPa.

the boundary of the torque arm (see Fig. 9). In order to maintain symmetric geometry, design parameters are linked. As design parameters are changed, a new shape density for each finite element is calculated from which the material constants are changed as depicted in (3).

Since there is no analytical solution, it is difficult to verify the accuracy of the sensitivity results. As a second resort, they can be compared with the sensitivity results obtained from the finite difference method. This approach by no means guarantees the accuracy of sensitivity results. It assures consistency with the numerical method employed. The finite difference method perturbs the design variable with a small amount ($\Delta\tau$) and solves the structural problem again. The sensitivity can then be approximated by

$$\psi' \approx \frac{\Delta\psi}{\Delta\tau} = \frac{\psi(u+\Delta\tau) - \psi(u)}{\Delta\tau}, \tag{45}$$

where u is the current design value and $u + \Delta\tau$ is the perturbed design value. This process must be repeated for each design variable.

Table 1 shows the comparison of the sensitivity results with the finite difference results. A small perturbation of $\Delta\tau = 10^{-4}$ is used. Since there are eight design variables, the finite difference method needs to perturb the design eight times and solves the structural problem repeatedly. Three different types of performance functions are considered: structural area, maximum von Mises stress, and y-directional displacement at the location (10, 0). In Table 1, the first column is the design variable, the second column is the performance type and its value, the third column is the performance change calculated from the finite difference method, the fourth column is the performance change estimated from the proposed sensitivity

Table 1
Design sensitivity results are compared with finite difference sensitivity results (perturbation size = 0.0001)

Design		ψ	$\Delta\psi$	$\psi'\Delta\tau$	$\Delta\psi/\psi'\Delta\tau \times 100\%$
u_1	Area	3.749200e+02	1.036225e−04	1.036146e−04	100.01
	σ_{MAX}	2.484748e+02	−6.082722e−04	−6.084701e−04	99.97
	z_y	9.215100e−02	−1.237382e−07	−1.237448e−07	99.99
u_2	Area	3.749200e+02	3.566629e−03	3.566612e−03	100.00
	σ_{MAX}	2.484748e+02	−2.092790e−02	−2.094751e−02	99.91
	z_y	9.215100e−02	−4.259725e−06	−4.259550e−06	100.00
u_3	Area	3.749200e+02	1.011942e−04	1.011766e−04	100.02
	σ_{MAX}	2.484748e+02	−2.957883e−05	−2.937141e−05	100.71
	z_y	9.215100e−02	−1.231901e−08	−1.231175e−08	100.06
u_4	Area	3.749200e+02	3.482701e−03	3.482692e−03	100.00
	σ_{MAX}	2.484748e+02	−1.010746e−03	−1.011070e−03	99.97
	z_y	9.215100e−02	−4.238100e−07	−4.237938e−07	100.00
u_5	Area	3.749200e+02	1.999743e−04	1.999999e−04	99.99
	σ_{MAX}	2.484748e+02	−3.757007e−04	−3.758011e−04	99.97
	z_y	9.215100e−02	−3.233982e−07	−3.234727e−07	99.98
u_6	Area	3.749200e+02	−1.654841e−03	−1.654802e−03	100.00
	σ_{MAX}	2.484748e+02	3.386682e−03	3.386067e−03	100.02
	z_y	9.215100e−02	7.485533e−07	7.484632e−07	100.01
u_7	Area	3.749200e+02	−2.000052e−04	−1.999999e−04	100.00
	σ_{MAX}	2.484748e+02	5.511106e−04	5.510200e−04	100.02
	z_y	9.215100e−02	3.767109e−07	3.766835e−07	100.01
u_8	Area	3.749200e+02	−1.654854e−03	−1.654803e−03	100.00
	σ_{MAX}	2.484748e+02	2.847409e−03	2.847083e−03	100.01
	z_y	9.215100e−02	1.359770e−06	1.359566e−06	100.01

results, and the last column is the ratio between the third and fourth columns. Table 1 shows an excellent agreement between the two methods. Thus, the proposed sensitivity calculation method can be used for gradient calculation during optimization. The biggest advantage of the proposed method is its computational efficiency. The cost of sensitivity calculation is less than 5% of the structural analysis cost per design variable. Thus, the proposed method can significantly reduce the design cost.

A simple design optimization problem is proposed to minimize the area of the structure, while satisfying the maximum stress constraint. In order to induce large shape change, a loose constraint limit is deliberately provided. Thus, the design optimization problem can be stated as

$$\begin{cases} \text{Minimize} & \dfrac{\text{area}}{A_0} \\ \text{Subject to} & \dfrac{\sigma_{\max}}{\sigma_0} - 1 \leqslant 0. \end{cases} \tag{46}$$

In (46), the cost function and constraint are normalized such that the cost function is one at the initial design and the constraint is zero at the optimum design. The lower and upper bounds of design parameters are selected such that the topology of the structure is maintained. For this particular example, $A_0 = 374.9\ \text{cm}^2$ and $\sigma_0 = 800$ MPa are used.

The design optimization problem is solved using the modified feasible direction method in the Design Optimization Tool (DOT) [27]. The advantage of this method is that it only moves within the feasible design so that every intermediate design satisfies the constraint. Function values and sensitivity information are provided to the gradient-based optimization algorithm. The design optimization problem converges after five design iterations. Table 2 shows the values of the design variables at the initial and optimum designs. All initial design variables start from zero so that the value of the design variable represents the change of the dimension from the initial design. Two design variables are on the boundary, five design variables are very close to the boundary, and u_8 is in the middle of design domain. The lower and upper bounds are selected such that the topology of the structure is maintained.

Fig. 11 shows the shape density and stress contour plots at the optimum design. The optimization algorithm chose the geometry such that the maximum stress is evenly distributed along the upper and lower regions of the structure. The optimum design conforms in an engineering sense because in such a beam-like structure the moment of inertia needs to be increased as the moment arm increases. Fig. 12 shows the scaled history plot of cost and constraint functions. The optimum design reduces more than 52% of the structural area. The maximum stress at the optimum design appears to be 800 MPa. Even if the design converges in the fifth iteration, the structural analysis has been performed fifty four times. This is because the modified feasible direction method requires many line searches.

The same optimization problem has been solved using many different approaches. For example, when Lagrangian finite element analysis is used with a re-meshing process [4], the optimization process converged at 45 iterations with eight re-meshing processes. In addition, when the Lagrangian meshfree method is used

Table 2
Design variables at the initial and optimum designs

Design	Lower bound	Initial design	Optimum design	Upper bound
u_1	−3.000	0.0	−2.99966	1.000
u_2	−0.500	0.0	−0.500	1.000
u_3	−1.000	0.0	−0.999722	1.000
u_4	−2.700	0.0	−2.69769	1.000
u_5	−5.500	0.0	−5.49977	1.000
u_6	−0.500	0.0	2.000	2.000
u_7	−1.000	0.0	5.99949	6.000
u_8	−0.500	0.0	−0.238489	0.000

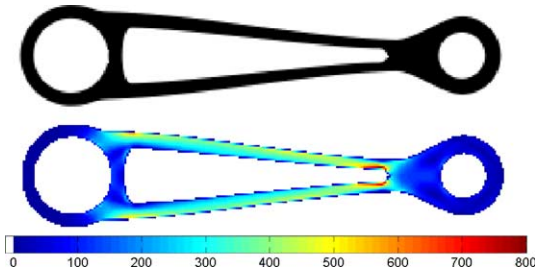

Fig. 11. Finite element analysis results at the optimum design. Unit: MPa.

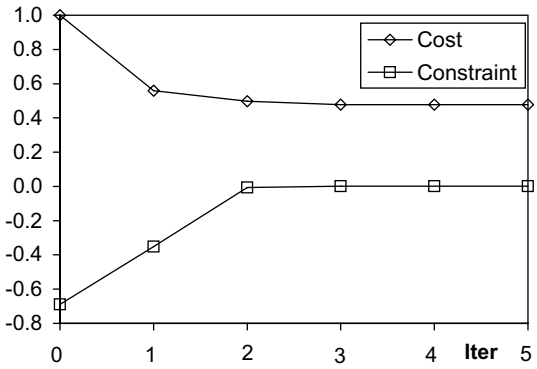

Fig. 12. Design optimization history for (normalized) cost and constraint functions.

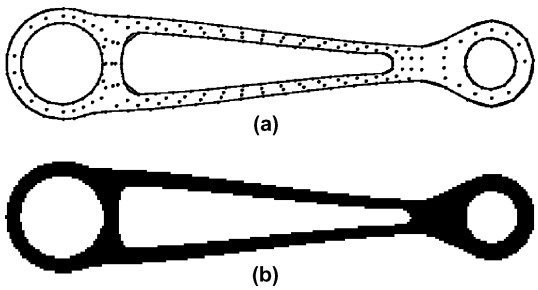

Fig. 13. Comparison of optimum designs. (a) Optimum design using Lagrangian approach and (b) optimum design using Eulerian approach.

[24], the optimization problem converged at 20 iterations. All three methods converged to a similar optimum design, as illustrated in Fig. 13.

6.3. Bracket model

The second example is the bracket model, as shown in Fig. 14. Two holes in the bottom are fixed in space, while a horizontal force of 15,000 N is applied at the center of the upper hole. The same material property has been used with the torque arm problem. A rectangular domain is established with the lower-left corner being $(-8,-1)$ and the upper-right corner being $(8,20)$, which covers the whole structure.

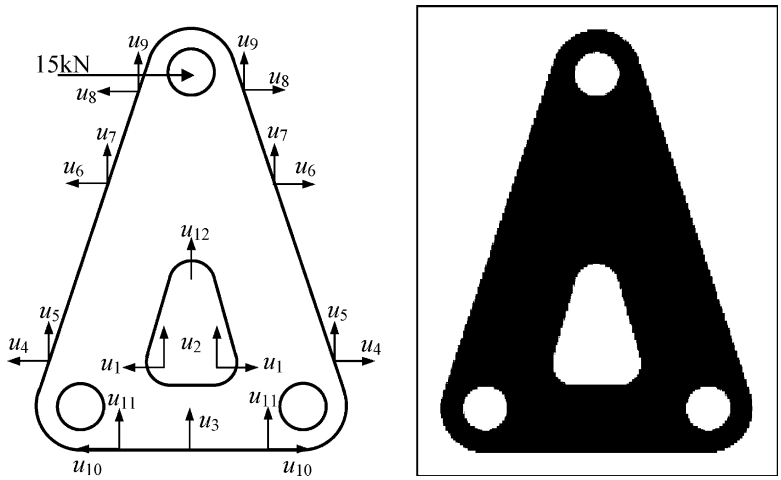

Fig. 14. Design parameterization and boundary homogenization of the bracket with pixel size = 0.11 cm.

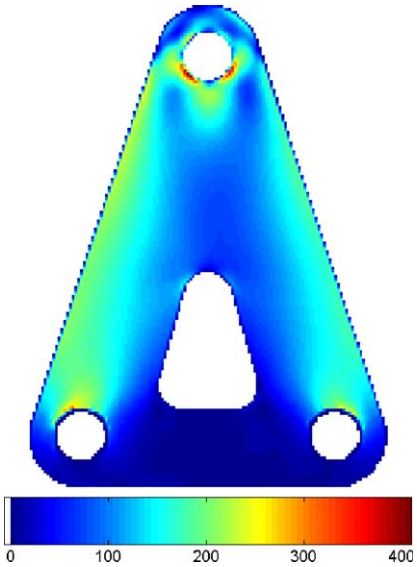

Fig. 15. Finite element analysis results of the bracket (equivalent stress plot). Unit: MPa.

Square finite elements (size = 0.11 cm × 0.11 cm) are used to discretize the domain. Thus, the total grid size is 146 × 191, and the total degrees-of-freedom are 56,448. The structural analysis took 19.0 s for solving the matrix equation using a 1.2 GHz laptop computer. Fig. 15 shows the von Mises stress contour plot at the initial design of the bracket model.

As is shown in Fig. 14, twelve design parameters have been selected to change the inner/outer boundary of the bracket, while maintaining symmetry. Three performance functions have been chosen: area, maximum stress, and x-directional displacement at the location (0.37, 14.15). Since the number of design variables is greater than the number of performance measures, it is clear that the adjoint variable method would be more efficient than the direct differentiation method. The sensitivity coefficients for the three

performances are calculated using the adjoint variable method. It took 5.4 s for the design sensitivity analysis. If the finite difference method is employed, it is $19\,\mathrm{s} \times 12 = 228\,\mathrm{s}$ for calculating sensitivity information without considering the design perturbation effort. Thus, the proposed sensitivity calculation method is quite efficient.

Table 3 shows the sensitivity results compared to the finite difference results. For the finite difference method, a perturbation size of $\Delta\tau = 10^{-4}$ is employed. The second column ψ represents the performance value at the initial design; the third column represents the performance change estimated from the finite difference method; the fourth column represents the performance change estimated from the sensitivity

Table 3
Design sensitivity results are compared with finite difference sensitivity results (perturbation size = 0.0001)

Design		ψ	$\Delta\psi$	$\psi'\Delta\tau$	$\Delta\psi/\psi'\Delta\tau \times 100\%$
u_1	Area	1.452729e+02	−6.048413e−04	−6.048400e−04	100.00
	σ_{MAX}	4.100496e+02	7.123357e−07	7.122662e−07	100.01
	z_x	1.731155e−02	1.677348e−08	1.677140e−08	100.01
u_2	Area	1.452729e+02	2.916115e−04	2.916118e−04	100.00
	σ_{MAX}	4.100496e+02	7.314450e−07	7.313131e−07	100.02
	z_x	1.731155e−02	2.852526e−10	2.851279e−10	100.03
u_3	Area	1.452729e+02	−4.499358e−04	−4.499347e−04	100.00
	σ_{MAX}	4.100496e+02	−1.712231e−07	−1.712719e−07	99.97
	z_x	1.731155e−02	−1.829742e−10	−1.829556e−10	100.01
u_4	Area	1.452729e+02	1.068117e−03	1.068115e−03	100.00
	σ_{MAX}	4.100496e+02	3.249783e−06	3.247563e−06	100.07
	z_x	1.731155e−02	−3.614318e−07	−3.614374e−07	100.00
u_5	Area	1.452729e+02	3.555796e−04	3.555831e−04	100.00
	σ_{MAX}	4.100496e+02	1.083351e−06	1.081315e−06	100.19
	z_x	1.731155e−02	−1.203238e−07	−1.203252e−07	100.00
u_6	Area	1.452729e+02	1.170124e−03	1.170127e−03	100.00
	σ_{MAX}	4.100496e+02	−1.666535e−03	−1.666363e−03	100.01
	z_x	1.731155e−02	−2.674115e−07	−2.674292e−07	99.99
u_7	Area	1.452729e+02	3.895439e−04	3.895433e−04	100.00
	σ_{MAX}	4.100496e+02	−5.547770e−04	−5.547374e−04	100.01
	z_x	1.731155e−02	−8.902625e−08	−8.902916e−08	100.00
u_8	Area	1.452729e+02	4.320476e−04	4.320467e−04	100.00
	σ_{MAX}	4.100496e+02	−1.557322e−02	−1.557651e−02	99.98
	z_x	1.731155e−02	1.129704e−08	1.129773e−08	99.99
u_9	Area	1.452729e+02	1.438321e−04	1.438314e−04	100.00
	σ_{MAX}	4.100496e+02	−5.185300e−03	−5.185555e−03	100.00
	z_x	1.731155e−02	3.761005e−09	3.761081e−09	100.00
u_{10}	Area	1.452729e+02	0.000000e+00	1.127218e−20	0.00
	σ_{MAX}	4.100496e+02	0.000000e+00	6.600613e−16	0.00
	z_x	1.731155e−02	0.000000e+00	−3.648030e−20	0.00
u_{11}	Area	1.452729e+02	−3.999396e−04	−3.999419e−04	100.00
	σ_{MAX}	4.100496e+02	−6.968617e−08	−6.967609e−08	100.01
	z_x	1.731155e−02	−6.246176e−11	−6.245705e−11	100.01
u_{12}	Area	1.452729e+02	−2.916109e−04	−2.916118e−04	100.00
	σ_{MAX}	4.100496e+02	3.804684e−06	3.801079e−06	100.09
	z_x	1.731155e−02	5.256567e−08	5.256648e−08	100.00

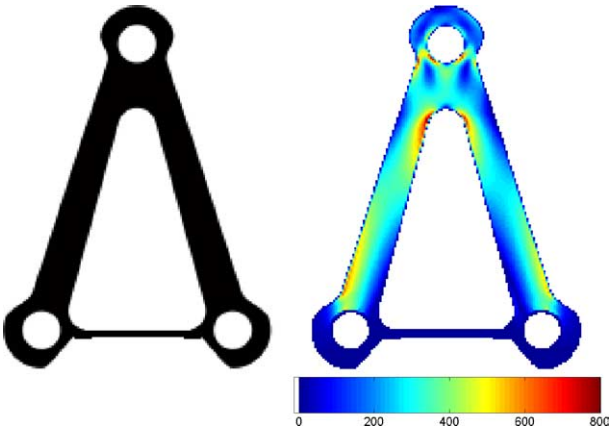

Fig. 16. Shape density and finite element analysis results at the optimum design. Unit: MPa.

coefficients; and the last column the ratio between the third and fourth columns. The two methods agree very well, as all ratios are very close to 100%.

The same design optimization problem as in (46) is used to minimize the area of the bracket structure. For this example, the sequential quadratic programming method is employed. The cost function (area) is normalized by $A_0 = 145\ \text{cm}^2$ and the constraint (max. von Mises stress) is normalized by $\sigma_0 = 800$ MPa, so that the active constraint should approach zero. Fig. 16 shows the shape density plot and the structural analysis results at the optimum design. The optimum design is significantly different from the initial design, as the size of the inner triangle increases. The maximum stress increases to the constraint boundary (800 MPa), so that the constraint becomes active. Table 4 shows the values of design variables at the initial and optimum designs. The lower and upper bounds are selected such that the structure maintains its topology during design optimization. All design variables start from zero, which means that the values of design variables depict the relative change of its coordinates.

Fig. 17 shows the design optimization history of cost and constraint functions. During the first six iterations, the cost function is significantly reduced until the constraint is activated. Next, nine iterations are carried out to further reduce the cost function, while keeping the constraint active. An attempt to further reduce the cost function at the 16th iteration caused the constraint violation. The remaining iterations are performed to overcome the violated constraint without reducing the cost function. The optimization con-

Table 4
Design variables at the initial and optimum designs

Design	Lower bound	Initial design	Optimum design	Upper bound
u_1	−0.900	0.0	1.600	1.600
u_2	−1.000	0.0	−1.000	1.500
u_3	−1.000	0.0	1.800	1.800
u_4	−1.000	0.0	−0.908	0.500
u_5	−0.200	0.0	−0.172	0.200
u_6	−0.800	0.0	−0.800	0.600
u_7	−0.200	0.0	−0.200	0.200
u_8	−1.000	0.0	−0.936	0.500
u_9	−0.200	0.0	−0.196	0.200
u_{10}	−0.800	0.0	−0.500	0.000
u_{11}	−1.000	0.0	1.800	1.800
u_{12}	−1.000	0.0	5.150	5.500

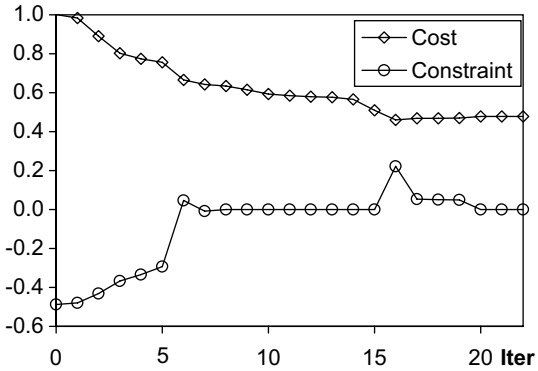

Fig. 17. Design optimization history for (normalized) cost and constraint functions.

verged at the 22nd iteration. The cost function is reduced by 62% of the original value. The increased height of the inner triangle (u_{12}) produces the most significant reduction in structural area, until the stress constraint is activated at the side frame. The maximum stress value, located at the top of the inner triangle, moves to the side frame at 800 MPa. A total of 32 response analyses and 22 sensitivity analyses were carried out during 22 optimization iterations. If we consider that the cost of three sensitivity analyses is equivalent to one structural analysis, the total optimization cost is less than 40 structural analyses, which is a significant reduction compared to 300 structural analyses when finite difference sensitivity is used. When the Lagrangian approach is used with the re-meshing process [4], the optimization process converges at 34 iterations with seven re-meshing processes. When the meshfree method [24] is employed, the optimization problem converges with seventeen iterations and 37 function evaluations. Thus, the Eulerian approach performs more design iterations, but the number of structural analyses is slightly smaller than with the meshfree method. The optimum cost function of the Eulerian approach is about 1.5% smaller than that of the meshfree method.

7. Conclusions

A new domain approximation method using an Eulerian description is developed for the structural optimization problem. Boundary homogenization provides a unique approximation of the structural domain and boundary on the fixed grid of finite elements. Design parameterization on the geometric model provides accurate representation of design intent, and the shape density concept resolves the mesh distortion problem that exists in the Lagrangian approach. Transformation of the design velocity field into a shape density variation plays a key role in making this approach possible. The main contribution of the current work is that the shape design sensitivity analysis involved in geometry changes is transformed into a parameter sensitivity analysis problem.

In order to become a practical engineering tool, the proposed approach needs to be extended to three-dimensional structures, which involves boundary homogenization of a volume. As the degrees-of-freedom of the system increase significantly, the need for an iterative solver will definitely be more pronounced.

Acknowledgement

The authors thank Prof. M.P. Bendsøe for his valuable comments and discussions.

References

[1] R.T. Haftka, R.V. Grandhi, Structural shape optimization—a survey, Comput. Methods Appl. Mech. Engrg. 57 (1) (1986) 91–106.

[2] E. Hardee, K.H. Chang, J. Tu, K.K. Choi, I. Grindeanu, X.M. Yu, A CAD-based design parameterization for shape optimization of elastic solids, Adv. Engrg. Software 30 (3) (1999) 185–199.

[3] N. Olhoff, M.P. Bendsøe, J. Rasamussen, On CAD-integrated structural topology and design optimization, Comput. Methods Appl. Mech. Engrg. 89 (1991) 259–279.

[4] J.A. Bennett, M.E. Botkin, Structural shape optimization with geometric description and adaptive mesh refinement, AIAA J. 23 (3) (1985) 458–464.

[5] K. Suzuki, N. Kikuchi, A homogenization method for shape and topology optimization, Comput. Methods Appl. Mech. Engrg. 93 (3) (1991) 291–318.

[6] M.P. Bendsøe, Optimization of Structural Topology, Shape, and Material, Springer-Verlag, Berlin, Heidelberg, 1995.

[7] M.J. García, G.P. Steven, Fixed grid finite elements in elasticity problems, Engrg. Comput. 16 (2) (1999) 145–164.

[8] M.J. García, G.P. Steven, Fixed grid finite element analysis in structural design and optimization, Proc. 2nd ASMO/AIAA Internet Conf. Approx. Fast Reanal. Engrg. Optim., 2000. Available from: <http://www-tm.wbmt.tudelft.nl/~wbtmavk/2aro_conf>.

[9] K. Horimatsu, N. Kikuchi, A shape optimization method based on fixed grid analysis, IACM Third World Congress in Computational Mechanics, 1994, vol. II, pp. 1070–1071.

[10] S.Y. Woon, L. Tong, O.M. Querin, G.P. Steven, Knowledge-based algorithms in fixed-grid GA shape optimization, Int. J. Numer. Methods Engrg. 58 (2003) 643–660.

[11] H. Kim, O.M. Querin, G.P. Steven, Y.M. Xie, Improving efficiency of evolutionary structural optimization by implementing fixed grid mesh, Struct. Multidisc. Optim. 24 (2003) 441–448.

[12] K.K. Choi, K.H. Chang, A study of design velocity field computation for shape optimal design, Finite Elem. Anal. Des. 15 (1994) 317–341.

[13] R.R. Salagame, A.D. Belegundu, Distortion, degeneracy and rezoning in finite elements—a survey, Sadhana—Acad. Proc. Engrg. Sci. 19 (1994) 311–335.

[14] O.C. Zienkiewicz, J.Z. Zhu, Adaptivity and mesh generation, Int. J. Numer. Methods Engrg. 32 (4) (1991) 783–810.

[15] J. Sienz, E. Hinton, Reliable structural optimization with error estimation adaptivity and robust sensitivity analysis, Comput. Struct. 64 (1–4) (1997) 31–63.

[16] K. Terada, T. Miura, N. Kikuchi, Digital image-based modeling applied to the homogenization analysis of composite materials, Comput. Mech. 20 (4) (1997) 331–346.

[17] O. Sigmund, A 99 line topology optimization code with the Matlab, Struct. Multidisc. Optim. 21 (2001) 120–127.

[18] T.J.R. Hughes, The Finite Element Method Linear Static and Dynamic Finite Element Analysis, Prentice-Hall, Englewood Cliffs, NJ, 1987.

[19] B.W. Clark, D.C. Anderson, The penalty boundary method, Finite Elem. Anal. Des. 39 (2003) 387–401.

[20] T. Belytschko, Y.Y. Lu, L. Gu, Element-free Galerkin methods, Int. J. Numer. Methods Engrg. 37 (2) (1994) 229–256.

[21] T.A. Davis, UMFPACK 4.1 User Guide, Univ. of Florida, 2003.

[22] K.K. Choi, E.J. Haug, Shape design sensitivity analysis of elastic structures, J. Struct. Mech. 11 (1983) 231–269.

[23] E.J. Haug, K.K. Choi, Methods of Engineering Mathematics, Prentice-Hall, Englewood Cliffs, NJ, 1993.

[24] N.H. Kim, K.K. Choi, M.E. Botkin, Numerical method for shape optimization using meshfree method, Struct. Multidisc. Optim. 24 (6) (2003) 418–429.

[25] G.W. Jang, Y.Y. Kim, K.K. Choi, Remesh-free shape optimization using the wavelet-Galerkin method, Int. J. Solids Struct. 41 (22–23) (2004) 6465–6483.

[26] P. Duysinx, M.P. Bendsøe, Topology optimization of continuum structures with local stress constraints, Int. J. Numer. Methods Engrg. 43 (1998) 1453–1478.

[27] G.N. Vanderplaats, DOT User's Manual, VMA Corp., 1997.